IEEE Photonics Journal
An IEEE Photonics Society Publication

Open Access

Plasmonic Holographic Metasurfaces for Generation of Vector Optical Beams

Volume 9, Number 1, February 2017

Jing Wen
Hui Feng
Jiannong Chen
Kang Wang
Yating Lv
Yangwan Zhong
Dawei Zhang

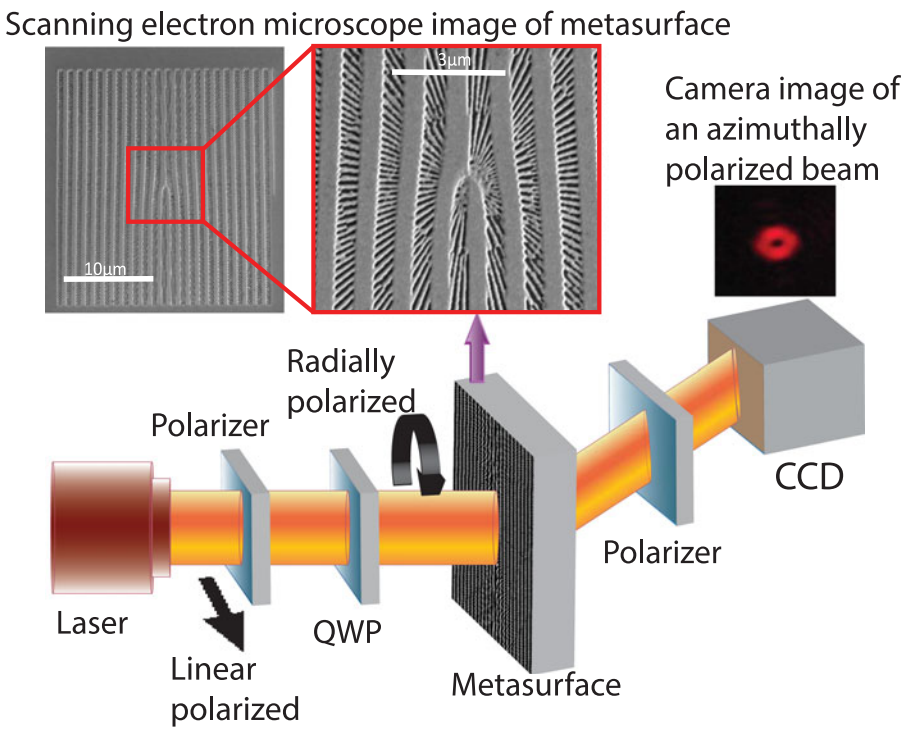

DOI: 10.1109/JPHOT.2017.2651981
1943-0655 © 2017 IEEE

IEEE photonics SOCIETY

IEEE

Plasmonic Holographic Metasurfaces for Generation of Vector Optical Beams

Jing Wen,[1] Hui Feng,[1] Jiannong Chen,[1,2] Kang Wang,[1] Yating Lv,[1] Yangwan Zhong,[1] and Dawei Zhang[1]

[1]Engineering Research Center of Optical Instrument and Systems, Ministry of Education and Shanghai Key Laboratory of Modern Optical Systems, University of Shanghai for Science and Technology, Shanghai 200093, China
[2]School of Physics and Optoelectronic Engineering, Ludong University, Yantai 264025, China

DOI:10.1109/JPHOT.2017.2651981

Manuscript received November 30, 2016; revised January 5, 2017; accepted January 7, 2017. Date of publication January 11, 2017; date of current version January 25, 2017. This work was supported in part by the National Basic Research Program of China (973 Program) under Grant 2015CB352001 and in part by the National Natural Science Foundation of China under Grant 61378060. Corresponding author: D. Zhang (e-mail: dwzhang@usst.edu.cn).

Abstract: In this paper, a 2-D anisotropic metasurface for generating an azimuthally polarized beam is structured with a patterned metallic layer, which is composed of a fork hologram and periodically aligned sector-shaped antennas in annular circles. The polarization state of the light is tailed due to the plasmonic effect of the antenna unit, which behaves like a single nanopolarizer. The induced Pancharatnam–Berry phase will be compensated by the fork hologram. Such a metasurface in a large pattern size of 27 by 27 μm with fine nanoaperture slits in a resolution of 200 nm is successfully fabricated. Numerical simulations of the single antenna element and the whole holographic structure are performed and coincide with experimental results well. An azimuthally polarized vector beam with a ring-shaped intensity distribution is generated by the metasurface from an incident circularly polarized light, which will serve as flat optical components in optical trapping, super-resolution imaging, and other application fields.

Index Terms: Surface plasmons, metasurfaces, vectorial optical beams, plasmonic antennas.

1. Introduction

Metasurfaces possess super abilities to manipulate light by tailoring and controlling polarizations, amplitudes, and phases of the waves [1]–[13] and open several application avenues such as wavefront shaping, characterization of polarization, and measurement of orbital angular momentum and other optical functional devices [14]–[17]. They are composed of artificial structures which have characteristic sizes smaller than the operating wavelength. Different from conventional optical elements and diffractive optical elements (ODEs), metasurfaces are based on surface plasmonic effects of nano-structures rather than accumulating optical paths from the optical materials. The precise control of phases of the waves allows the metasurfaces to act as abberation-free super lenses in optical, telecom and terahertz wavelengths [18], [19]. Huang [20], [21] demonstrated a three dimensional holography due to phase changes of a circular polarized beam scattered from plasmonic structures. Cui *et al.* proposed the coding or digital metamaterials which are able to

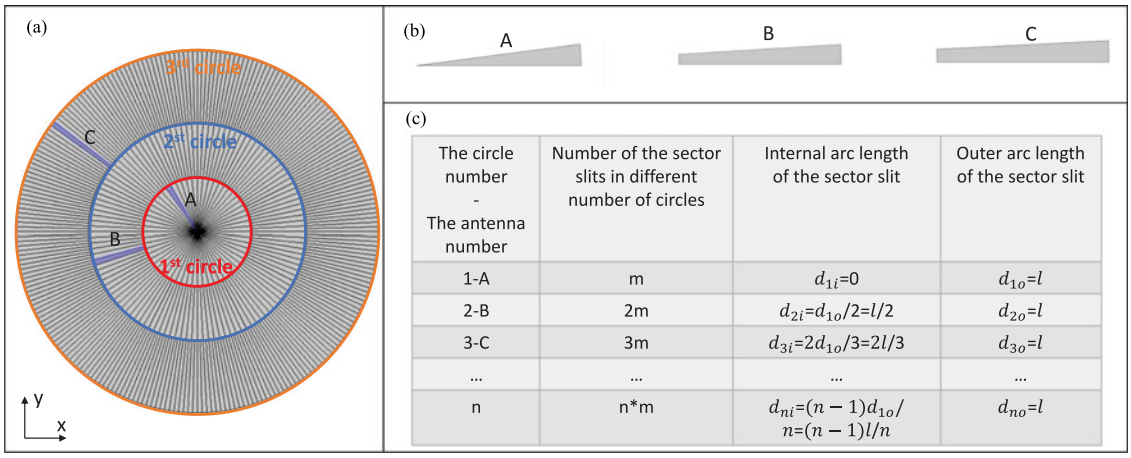

(c)

The circle number - The antenna number	Number of the sector slits in different number of circles	Internal arc length of the sector slit	Outer arc length of the sector slit
1-A	m	d_{1i}=0	d_{1o}=l
2-B	2m	d_{2i}=d_{1o}/2=l/2	d_{2o}=l
3-C	3m	d_{3i}=2d_{1o}/3=2l/3	d_{3o}=l
...	...	...	...
n	n*m	d_{ni}=$(n-1)d_{1o}$/ n=$(n-1)l/n$	d_{no}=l

Fig. 1. (a) Schematic view of arranged sector-shaped slit antennas in the architecture of three annular circles. Colored marked antennas as different antenna units in each circle. (b) Magnified colored marked antennas in (a). (c) Summary of geometric sizes for sector-shaped antennas in different annular circles.

manipulate the optical waves in different manners [22]–[25]. More interestingly, metasurfaces offer competitive methods to easily and precisely generate vectorial optical fields [26]–[29] compared to the previous conventional means such as spatial light modulators, optical cavities or other methods [28], [30]–[33]. For example, Yu *et al.* proposed a specially designed metasurface for generating vortex optical fields using V-shaped antennas [34]. A metasurface for converting an azimuthally polarized beam to a radially polarized light, which is then focused again to obtain an optical needle field [27]. Arbitrary spatial variations of phase and polarization of optical fields are realized by using rectangular nano-slits [26]. By varying the orientation of rectangular slits, the polarization of the transmitted light can be rotated according to the designed pattern. However, an additional Pancharatnam-Berry phase is induced at the same time with the rotational slits [35]. In order to compensate the helical phase, Lin combined a fork hologram with concentric metallic rings to obtain a radially polarized beam [36]. However, generating a high quality azimuthally polarized beam based on metasurfaces is still an interesting and challenge task and has yet to be realized.

In this paper, a holographic metasurface based on carefully aligned sector nano-slit plasmonic antennas is proposed to convert a circularly polarized light to an azimuthally polarized beam. Such a metasurface device is ultra-compact with a size of 27 μm by 27 μm, which has the ability to be designed even smaller in the future. The fabrication of such a metasurface is achievable by only one step etching process of focused ion beam milling. Our demonstrated metasurface provides a promising way to generate cylindrical vector beams with both high qualities and high efficiencies.

2. Structure Design of the Holographic Metasurface

A gold layer with densely arranged sector-shaped slit antenna elements in an architecture of different annular circles is introduced in our design in order to obtain a high quality azimuthally polarized beam. The antenna shape is different from Kang's rectangular slit antennas [35]. The schematic view of the sector-shaped slit antenna arrays in a specific alignment, which will be utilized in the holographic metasurface's design, is shown in Fig. 1(a). The whole area of the rotationally symmetric nano-pattern is separated to several subareas of neighboring annular rings which have the same central position. From the center of the circle to the outside direction, the circle is surrounded by annular rings one by one. These subareas are filled with periodic sector nano-slit arrays along the azimuthal direction. The outer arc lengths of the sector-slit antenna are always designed to be $l = 199$ nm, which is one third of the wavelength of the incident beam with $\lambda = 632.8$ nm. Since the radii of these circles are d, $2d$, and $3d$, respectively, with $d = 1.9\,\mu$m, the

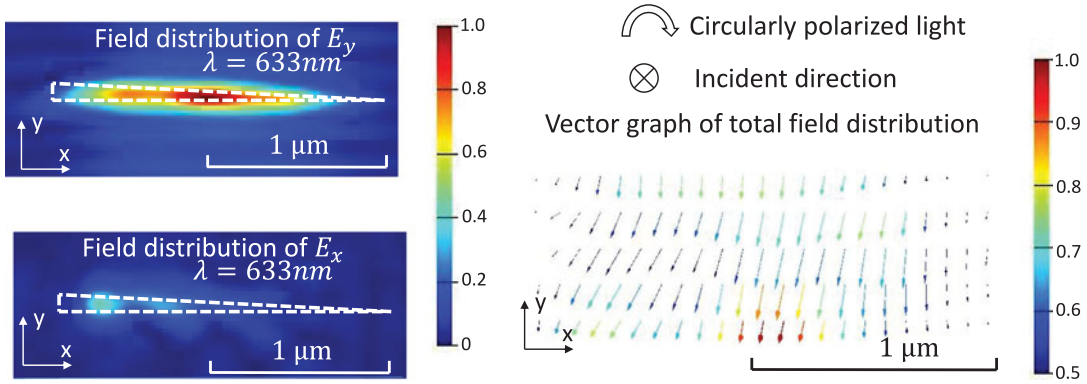

Fig. 2. Field distributions of E_y (a) and E_x (b) in xy detection plane which is 180 nm away from the bottom of the gold layer. (c) Vector graph of total field distributions.

number of the slit antennas in each annular circle are 60, 120 and 180. The magnified geometric shapes of the unit antenna marked in Fig. 1(a) with different colors are shown in Fig. 1(b). Although the outer arc length of each slit antenna is the same, the internal arc length is different for antennas lies in different annular circles as shown in the table in Fig. 1(c). It is well-regulated that the internal arc length of the sector-shaped antenna in the n_{th} circle ($n = 1, 2, 3...$) is equal to $d_{ni} = (n-1)l/n$ with $d_{1o} = l$. With the increasing number n, sector-shaped antennas will approach to rectangular slits.

The Finite-Difference Time-Domain simulations of the single sector-shaped slit element are performed by the commercial software Lumerical. The computation area has a size of $5\,\mu\text{m} \times 5\,\mu\text{m} \times 3\,\mu\text{m}$, and is surrounded by perfect matched layers (PMLs). A sector-shaped aperture antenna is embedded in a single gold layer with a thickness of 150 nm, which means the aperture region is filled with air. Above and below the gold layer is also surrounded by air. The geometric size of the antenna in the first circle is already listed in Fig. 1(c). The optical constant of gold is taken with reference of Palik's data. The mesh size of the aperture slit is refined to 2 nm. Fig. 2(a) and (b) represent the simulated electric near-field distributions of E_x and E_y of the light, which is transmitted through the unit cell antenna of A in Fig. 1(b) when the detection plane is 180 nm away from the bottom of the gold layer. The plasmonic mode is excited on the sidewalls of the boundaries of the sector slit antenna. Since there are two sidewalls nearby each other along the radius of the sector, the highly confined metal-air-metal plasmonic mode allows the sector slit antenna behaves like a nano linear polarizer, for which the polarization of the transmitted light is always perpendicular to the radius direction of the sector. It should be noticed that the sidewall of the outer arc of the sector also induces plasmonic modes, and the field distribution of E_x has a large value on the boundary of the outer arc of the antenna. The field strengths of E_x are much smaller than that of E_y, as shown in Fig. 2(b). Fig. 2(c) shows the vector graph of total field distributions on the detection plane, for which the lengths of the arrows are proportional to the field amplitudes whereas the directions of the arrows represent the polarizations of the fields. The bandwidth and the transmission efficiency of a single sector-antenna is calculated as shown in Fig. 3. The transmission is calculated by the transmitted power over the incident power, and then later is normalized to a factor, which is the ratio between the antenna area and the simulation domain in xy plane. An obvious extraordinary transmission is found, which is expected from the plasmonic effects. It can be seen in the figure that the transmission is optimized at the wavelength of 1 μm, and the full width half maximum of the transmission is 730 nm, which is ultra-broadband.

As is well known that the Jones matrix of a polarizer [35] can be described by

$$\mathbf{M} = \begin{pmatrix} \cos^2\alpha & \sin\alpha\cos\alpha \\ \sin\alpha\cos\alpha & \sin^2\alpha \end{pmatrix} \tag{1}$$

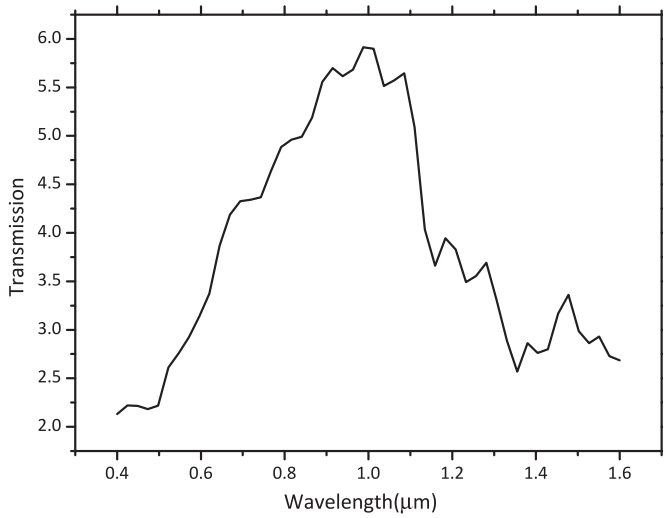

Fig. 3. Transmission of the light through the single antenna unit from the wavelength of 0.4 μm to 1.6 μm.

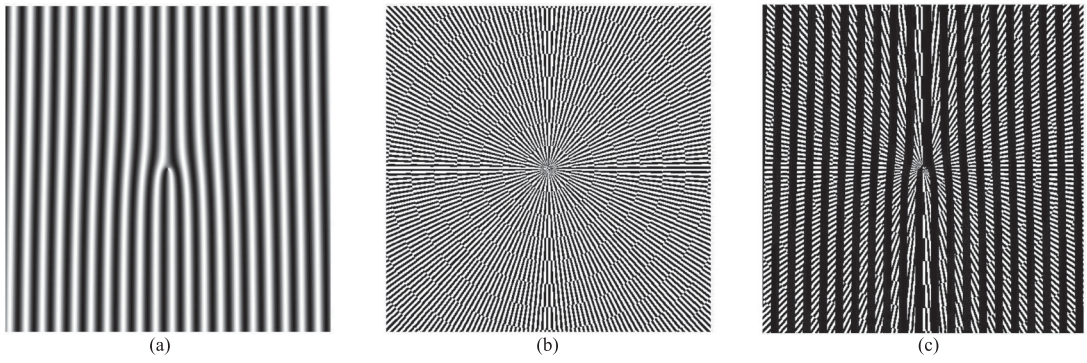

Fig. 4. (a) Computer generated fork hologram for generating a beam with a spiral phase. (b) Rotationally symmetric nano-pattern with periodic sector slit arrays for polarization filtering. (c) Binary holographic image, which is the superposition of the relatively large feature (a) and the nano-structuring pattern (b).

in which α is the angle between the polarization direction and x axis. If the incident field is circularly polarized, the light passed through the polarized can be described as

$$\mathbf{E} = \exp(\mp i\alpha)\begin{pmatrix}\cos\alpha\\ \sin\alpha\end{pmatrix}. \tag{2}$$

In (2), the positive and the negative signs are induced from right handed and left handed incident beams respectively. It can be seen that both the polarization and the phase of the transmitted light are changed according to the angle α. Suppose the sector-shaped antenna is considered as a linear polarizer, the aligned rotational antennas shown in Fig. 1(a) will induce an additional Pancharatnam-Berry phase.

In order to compensate the Pancharatnam-Berry phase, a fork hologram shown in Fig. 4(a) is designed and calculated. An object beam is a vortex beam which has a spiral phase with a topological charge of 1, a reference beam is a tilted incident plane wave with an intersection angle of 7° relative to the object beam, and the interference between the object beam and the reference beam results the fork hologram. It should be noticed that the spiral phase induced by the fork

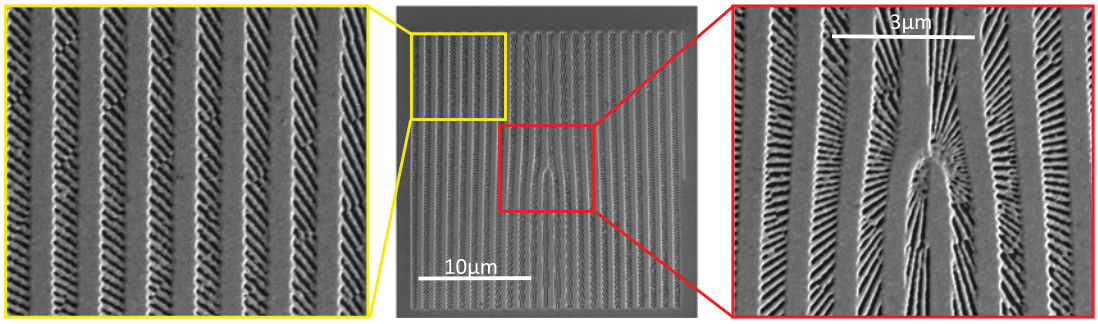

Fig. 5. Scanning electron microscopy image of the magnified corner area of the structure (a), the entire holographic structure with an array size of 27 μm by 27 μm (b), and the center area of the structure (c).

hologram [36] is conjugate to the Pancharatnam-Berry phase of the polarization filtering by the sector nano-slit array of the nano-pattern.

The holographic metasurface, which is shown in Fig. 4 is composed of the computer generated fork hologram with the relatively large structure and rotationally symmetric nano-slits in several annular rings. For the nano-slits in Fig. 1(a), grey pixel values of 0 and 255 are alternatively filled, which represent the subareas with the gold maintained and etched away respectively. Following the above design, there are m periods of the black and the white sector slits for the first annular ring in Fig. 4(b). It is deduced that $2m$ periods for the second annular ring, $3m$ periods for the third one and so on. Fig. 4(c) shows the binary holographic image, which is the superposition of the relatively large features in Fig. 4(a) and the nano-structuring pattern in Fig. 4(b). First, the pixel grey value of both the coarse and the fine patterned images are first normalized to the maximum value. Since the rotationally symmetric nano-structure pattern is a binary image for which the pixel has a grey value of either 0 or 255, the normalized value for each pixel will be either 0 or 1. Next, for each pixel position of the final holographic image, the pixel value is equal to the multiplied normalized pixel value between the coarse and the fine patterned images. Then the pixel value which is larger than 0.5 will convert to the value of 1, while the pixel value smaller than 0.5 will convert to 0. Finally, each pixel value will be multiplied by the value of 255, and re-scaled back to the normal 8 bit pixel value range.

3. Fabrication, Numerical Simulations and Experimental Results

For the fabrication of the sample, a 5 nm thick chromium layer and a 150 nm thick gold layer are deposited on top of a silica substrate by electronic beam evaporation machine, and the above binary holograph will be saved in a bmp format which is imported by the controlling software of the focused ion beam system(Helios Nanolab 600,FEI). During the ion beam milling process, it should be noticed that the white areas of the holographic image represent the hollow gaps in which the gold should be completely etched away, while the black areas of the image correspond to the region where the gold would be maintained. The fabricated sample with an array size of 27 μm by 27 μm is shown in Fig. 5(b), and the magnified corner and center areas of the structure are displayed in Fig. 5(a) and (c), respectively. It is clear that the plasmonic antenna array is fabricated in a high quality, except that in Fig. 5(c) only a few gold grains are clustered while other parts are over-etched. The factors induce such fabrication imperfections include the limit of the aspect ratio of the focused ion beam milling, and spatial drifts of the sample due to the long milling time for such a large structure array.

The experimental setup is shown in Fig. 6. The optical beam from the HeNe laser with the wavelength of 632.8 nm will be converted to a circular polarized beam through a polarizer and a quarter wave plate. The beam is then incident on the sample of the holographic metamaterial.

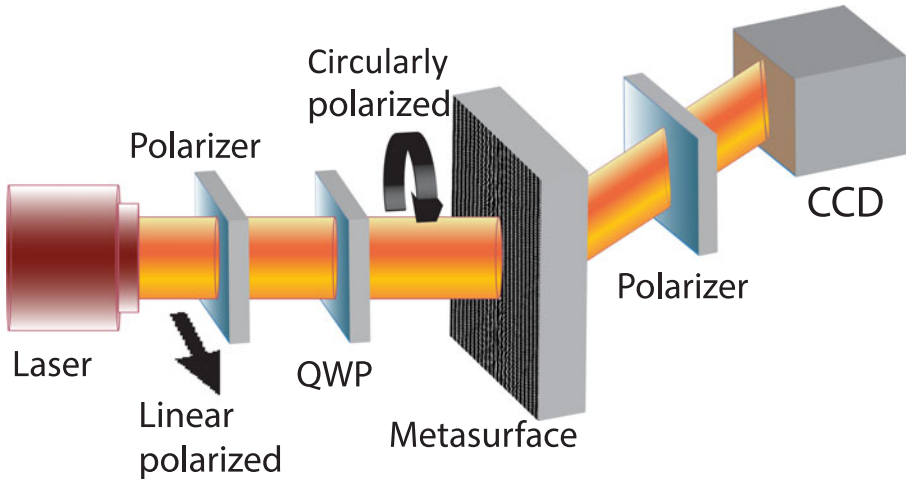

Fig. 6. HeNe laser with the wavelength of 632.8 nm passes through a polarizer (LP) and a quarter wave plate (QWP) to yield a circularly polarized light. Between the holographic metamaterial and the CCD camera, a linear polarizer is placed on the direction of the positive first order diffraction beam.

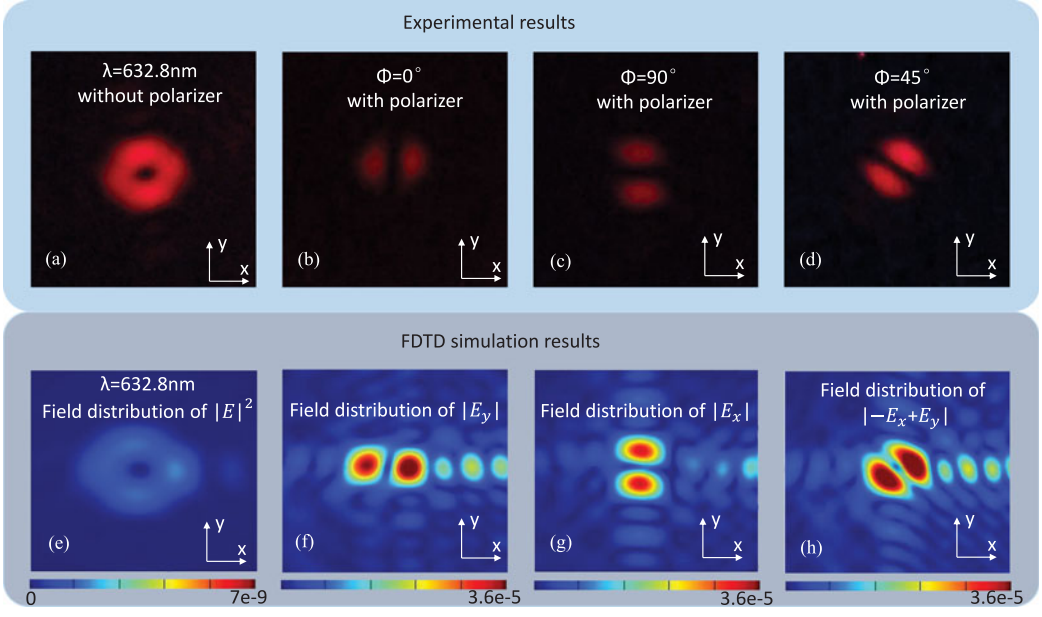

Fig. 7. Measured field intensity distributions of the first diffraction order beam through the holographic metasurface at the wavelength of 632.8 nm of (a) without polarizer in front of the camera and with polarizer direction of $\phi = 0^\circ$ (b), $\phi = 90^\circ$ (c), and $\phi = 45^\circ$ (d). Simulated field distributions of the total field intensity (e), $|E_y|$ (f), $|E_x|$ (g), and $|-E_x + E_y|$ (h) of the first positive diffraction order beam from the sample.

The positive first order diffraction beam through the sample is filtered by a linear polarizer and then imaged by a CCD camera which is placed around 30 cm away from the sample. The measured field intensity distributions of the output beam through the holographic nano-structured metamaterial are detected by the CCD camera without the linear polarizer in Fig. 7(a), which shows a typical hollow intensity distribution of a cylindrical vector beam. Fig. 7(b), (c), and (d) indicate the field distributions of the beam after being filtered by the linear polarizer with direction angles of $\phi = 0^\circ$, 90° and 45°, respectively. The fields of two lobes rotate correspondingly with the change of the polarizer direction,

and it is demonstrated that the generated beam is a high quality optical field of an azimuthally polarized vector beam.

In order to demonstrate the concept further and compare with the experimental results, the graph of Fig. 4(c) is imported to the commercial software Lumerical for the Finite-Difference Time-Domain simulation. The two dimensional boundary information is extracted from the graph, and is then extruded with a thickness of 150 nm. The computation area has a size of 28 μm $\times$ 28 μm $\times$ 3 μm. The mesh size of the aperture slit is refined to 2 nm. The near field distributions on the plane which is 180 nm away from the bottom of the layer are saved, and are then converted to far field distributions on a semi-sphere with a radius of 1 m for which the center matches the middle point of the sample. The default far field projection functions in the commercial toolbox of Lumerical are used to obtain the far field distributions. The near field data is decomposed of a set of plane waves propagating at different angles, and an efficient algorithm is used to calculate the electric fields in the far field regions. The distributions of the total field intensity $|E_x|$, $|E_y|$ and $|-E_x+E_y|$ of the first positive diffraction order beam are exhibited in Fig. 7(e), (f), (g), and (h), respectively, which are coincident with the experimental results well. One reason for the slight imperfection in Fig. 7(e) is probably that the structure in the image is pixelized and discrete rather than perfect continuous features.

4. Conclusion

In conclusion, a holographic metasurface with specially aligned sector-shaped plasmonic antennas which can generate an azimuthally polarized vector beam from an incident circularly polarized light is demonstrated both numerically and experimentally. The positive first order diffracted beam presents a ring-shaped intensity distribution. Such a metasurface provides a convenient way to produce a vector beam with a minimized flat optical component, which will have an extensive application in optical trapping, nano-manipulation, super-resolution imaging, etc.

References

[1] N. Yu and F. Capasso, "Flat optics with designer metasurfaces," *Nature Mater.*, vol. 13, pp. 139–150, 2014.
[2] G. X. Li *et al.*, "Spin-enabled plasmonic metasurfaces for manipulating orbital angular momentum of light," *Nano Lett.*, vol. 13, no. 9, pp. 4148–4151, 2013.
[3] A. V. Kildishev, A. Boltasseva, and V. M. Shalaev, "Planar photonics with metasurfaces," *Science*, vol. 339, pp. 1232009:1–6, 2012.
[4] N. Yu *et al.*, "Flat optics: Controlling wavefronts with optical antenna metasurfaces," *IEEE J. Sel. Topics Quantum Electron.*, vol. 19, no. 3, pp. 4700423–4700423, May 2013.
[5] Z. Wei, Y. Cao, X. Su, Z. Gong, Y. Long, and H. Li, "Highly efficient beam steering with a transparent metasurface," *Opt. Exp.*, vol. 21, no. 9, pp. 10739–10745, May 2013.
[6] J. Xiang *et al.*, "Polarization beam splitters, converters and analyzers based on a metasurface composed of regularly arranged silicon nanospheres with controllable coupling strength," *Opt. Exp.*, vol. 24, no. 11, pp. 11 420–11 434, May 2016.
[7] G. Minatti, F. Caminita, E. Martini, M. Sabbadini, and S. Maci, "Synthesis of modulated-metasurface antennas with amplitude, phase, and polarization control," *IEEE Trans. Antennas Propag.*, vol. 64, no. 9, pp. 3907–3919, Sep. 2016.
[8] C. P. Scarborough, D. H. Werner, and D. E. Wolfe, "Compact low-profile tunable metasurface-enabled antenna with near-arbitrary polarization," *IEEE Trans. Antennas Propag.*, vol. 64, no. 7, pp. 2775–2783, Jul. 2016.
[9] E. Erfani, M. Niroo-Jazi, and S. Tatu, "A high-gain broadband gradient refractive index metasurface lens antenna," *IEEE Trans. Antennas Propag.*, vol. 64, no. 5, pp. 1968–1973, May 2016.
[10] Y. Fan *et al.*, "In-plane feed antennas based on phase gradient metasurface," *IEEE Trans. Antennas Propag.*, vol. 64, no. 9, pp. 3760–3765, Sep. 2016.
[11] S. Pandi, C. A. Balanis, and C. R. Birtcher, "Design of scalar impedance holographic metasurfaces for antenna beam formation with desired polarization," *IEEE Trans. Antennas Propag.*, vol. 63, no. 7, pp. 3016–3024, Jul. 2015.
[12] S. Campione, D. de Ceglia, C. Guclu, M. A. Vincenti, M. Scalora, and F. Capolino, "Fano collective resonance as complex mode in a two-dimensional planar metasurface of plasmonic nanoparticles," *Appl. Phys. Lett.*, vol. 105, no. 19, 2014, Art. no. 191 107.
[13] J. Li *et al.*, "Simultaneous control of light polarization and phase distributions using plasmonic metasurfaces," *Adv. Functional Mater.*, vol. 25, no. 5, pp. 704–710, 2015.
[14] D. Wen *et al.*, "Metasurface for characterization of the polarization state of light," *Opt. Exp.*, vol. 23, no. 8, p. 10272, 2015.
[15] X. Chen, H. Zhou, M. Liu, and J. Dong, "Measurement of orbital angular momentum by self-interference using a plasmonic metasurface," *IEEE Photon. J.*, vol. 8, no. 1, pp. 1–8, Feb. 2016.

[16] D. Veksler, E. Maguid, N. Shitrit, D. Ozeri, V. Kleiner, and E. Hasman, "Multiple wavefront shaping by metasurface based on mixed random antenna groups," *ACS Photon.*, vol. 2, no. 5, pp. 661–667, 2015.
[17] A. Pors, M. G. Nielsen, R. L. Eriksen, and S. I. Bozhevolnyi, "Broadband focusing flat mirrors based on plasmonic gradient metasurfaces," *Nano Lett.*, vol. 13, no. 2, pp. 829–834, 2013.
[18] M. Khorasaninejad, W. T. Chen, R. C. Devlin, J. Oh, A. Y. Zhu, and F. Capasso, "Metalenses at visible wavelengths: Diffraction-limited focusing and subwavelength resolution imaging," *Science*, vol. 352, no. 6290, pp. 1190–1194, 2016.
[19] X. Yan *et al.*, "Broadband, wide-angle, low-scattering terahertz wave by a flexible 2-bit coding metasurface," *Opt. Exp.*, vol. 23, no. 22, pp. 29 128–29 137, Nov. 2015.
[20] L. Huang *et al.*, "Three-dimensional optical holography using a plasmonic metasurface," *Nature Commun.*, vol. 4, Nov. 2013, Art. no. 2808.
[21] G. Zheng, H. Mühlenbernd, M. Kenney, G. Li, T. Zentgraf, and S. Zhang, "Metasurface holograms reaching 80% efficiency," *Nature Nanotechnol.*, vol. 10, no. 4, pp. 308–312, 2015.
[22] S. Liu *et al.*, "Convolution operations on coding metasurface to reach flexible and continuous controls of terahertz beams," *Adv. Sci.*, vol. 3, no. 10, pp. 1–12, 2016.
[23] S. Liu *et al.*, "Anisotropic coding metamaterials and their powerful manipulation of differently polarized terahertz waves," *Light: Sci. Appl.*, vol. 5, 2016, Art. no. e16076.
[24] T.-J. Cui, S. Liu, and L.-L. Li, "Information entropy of coding metasurface," *Light: Sci. Appl.*, vol. 5, 2016, Art. no. e16172.
[25] T. J. Cui, M. Q. Qi, X. Wan, J. Zhao, and Q. Cheng, "Coding metamaterials, digital metamaterials and programming metamaterials," *Light: Sci. Appl.*, vol. 3, 2014, Art. no. e218.
[26] P. Yu *et al.*, "Generation of vector beams with arbitrary spatial variation of phase and linear polarization using plasmonic metasurfaces," *Opt. Lett.*, vol. 40, no. 14, pp. 3229–3232, 2015.
[27] S. Wang, D. C. Abeysinghe, and Q. Zhan, "Generation of vectorial optical fields with slot-antenna-based metasurface," *Opt. Lett.*, vol. 40, no. 20, pp. 4711–4714, 2015.
[28] G. Machavariani, Y. Lumer, I. Moshe, A. Meir, and S. Jackel, "Efficient extracavity generation of radially and azimuthally polarized beams," *Opt. Lett.*, vol. 32, no. 11, pp. 1468–1470, 2007.
[29] H. F. Ma, G. Z. Wang, G. S. Kong, and T. J. Cui, "Broadband circular and linear polarization conversions realized by thin birefringent reflective metasurfaces," *Opt. Mater. Exp.*, vol. 4, no. 8, pp. 1717–1724, 2014.
[30] S. Vyas, Y. Kozawa, and S. Sato, "Generation of radially polarized Bessel-Gaussian beams from c-cut Nd:YVO laser," *Opt. Lett.*, vol. 39, no. 4, pp. 1101–1104, 2014.
[31] P. Ma, P. Zhou, Y. Ma, X. Wang, R. Su, and Z. Liu, "Generation of azimuthally and radially polarized beams by coherent polarization beam combination," *Opt. Lett.*, vol. 37, no. 13, pp. 2658–2660, 2012.
[32] M. Eckerle *et al.*, "Novel thin-disk oscillator concept for the generation of radially polarized femtosecond laser pulses," *Opt. Lett.*, vol. 41, no. 7, pp. 1680–1683, 2016.
[33] B. G. Cai, Y. B. Li, W. X. Jiang, Q. Cheng, and T. J. Cui, "Generation of spatial bessel beams using holographic metasurface," *Opt. Exp.*, vol. 23, no. 6, pp. 7593–7601, Mar. 2015.
[34] N. Yu *et al.*, "Light propagation with phase discontinuities reflection and refraction," *Science*, vol. 334, no. 6054, pp. 333–337, Oct. 2011.
[35] M. Kang, J. Chen, X.-L. Wang, and H.-T. Wang, "Twisted vector field from an inhomogeneous and anisotropic metamaterial," *J. Opt. Soc. Amer. B*, vol. 29, no. 4, pp. 572–576, 2012.
[36] J. Lin, P. Genevet, M. A. Kats, N. Antoniou, and F. Capasso, "Nanostructured holograms for broadband manipulation of vector beams," *Nano Lett.*, vol. 13, no. 9, pp. 4269–4274, 2013.